Control of the visible and UV light water splitting and photocatalysis of nitrogen doped TiO$_2$ thin films deposited by reactive magnetron sputtering

Houssam Fakhouri [a,c,*], Jerome Pulpytel [a,c,*], Wilson Smith [a], Alireza Zolfaghari [b], Hamid Reza Mortaheb [b], Fateme Meshkini [b], Reza Jafari [b], Eliane Sutter [c], Farzaneh Arefi-Khonsari [a,c]

[a] Laboratoire de Génie des Procédés Plasma et Traitement de Surface, 11 Rue Pierre et Marie Curie, 75231 Paris, France
[b] Chemistry and Chemical Engineering Research Center of Iran, Tehran, Iran
[c] CNRS, UPR15, Laboratoire Interfaces et Systèmes Electrochimiques, 75005 Paris, France

ARTICLE INFO

ABSTRACT

N-doped TiO$_2$ thin films have been prepared by reactive RF magnetron sputtering at different pressures and with different compositions using a dual reactive gas mixture of nitrogen and oxygen. The morphological, optical, photo-electrochemical and photocatalytic properties have been studied in order to investigate the white light and visible light photoactivities of the films. Significant control over the band gap energy in the films was achieved by varying the deposition parameters. Photoelectrochemical characterization revealed improved white light photocurrent generation in nitrogen doped films prepared at low pressures. However, the visible light photocurrent generation showed improvement for all deposition pressures, and changed accordingly with the nitrogen incorporation. Photocatalytic measurements of a common chemical pollutant NMP (N-methyl-2-pyrrolidone) under different irradiation conditions provided evidence of improved photoactivity for samples prepared at high pressure, due to the increased active surface area and optimal nitrogen doping levels. Overall, this study showed a simple method to produce highly controllable nitrogen doping in different sites within TiO$_2$ showing improved visible light photoactivity and photo induced pollutant degradation. More interestingly, by investigating the effect of different nitrogen sites in nitrogen doped TiO$_2$, we have shown that the optimized conditions for photocatalysis do not correspond to those for water splitting.

© 2013 Elsevier B.V. All rights reserved.

1. Introduction

TiO$_2$ has shown extensive utilization in photocatalysts, dye-sensitized solar cells and smart-surface technologies. It is well known that the valance band of TiO$_2$ (having photo excited holes) is more positive than the O$_2$/H$_2$O redox potential, and the conductive band (containing the photo excited electrons) is lower than H$_2$/H$_2$O redox potential. The conductive band bottom determines the reduction potential of the photo excited electrons while the top of the valence band determines the oxidizing ability. However, the use of TiO$_2$ is limited to UV activation, due to its large band gap energy and relatively short electron–hole pair lifetime. Many

attempts have been made to address these two issues with varying success [1]. The primary efforts in extending the absorption range in TiO$_2$ from the UV range to the visible spectrum have focused on doping with non-metals. It has been reported that the band gap energy of TiO$_2$ could be narrowed by anion doping due to the mixing of the p states of the doped anion (N, S, C) with the O$_{2p}$ states of TiO$_2$, that could shift the resulted valence band edge upwards [2,3]. Asahi et al. established that nitrogen doping in TiO$_2$ should be the most effective method to improve visible light photoactivity, due to nitrogen's relatively small ionic radius (6% higher than that of oxygen) and optimal electronic band positions [2].

Early studies on N-doping within TiO$_2$ suggested that the nitrogen atoms hybridize with the valence band of the semiconductor, and this consequently results in a delocalization of the nitrogen valence electrons and resulted in an upward shift of the valence band maximum [4]. More recent density functional calculations have disputed this claim and suggested the formation of localized N$_{2p}$ states above the valence band of TiO$_2$. Density of state calculations has shown that substitutional N doping could exhibit one

isolated impurity level just 0.14 eV above the valence band energy [5]. However, interstitial N doping can also exhibit a localized impurity level at 0.73 eV higher than the valence band top [5]. In addition, interstitial NO and NO_2 doping have exhibited one or two isolated impurity levels in the middle of the band gap between the valence and conduction bands of TiO_2 [5,6] and these impurity levels could be hybridized with N_{2p} and O_{2p} states [7].

Experimentally, most nitrogen-doped TiO_2 exhibits visible light absorption as a shoulder in the visible wavelength (>400 nm) due to the formation of isolated N_{2p} orbitals above the valence band at lower nitrogen doping concentration ($N_{at} < 2\%$) into the TiO_2 lattice [8–10]. A smooth absorption shift toward visible light regions could be achieved in the case of higher concentration of nitrogen doping (up to 17%) [9,11]. The efficiency of doped TiO_2 under visible light strongly depends on the preparation method used. In some cases, such doped photocatalysts showed no activity under visible light [10] and/or lower activity in the UV spectral range compared to the non-doped TiO_2 [10,11]. This may be because of the increase in the carrier recombination rates due to the formation of defect states upon doping [10]. In non-metal doped TiO_2 photocatalysts, the main problem present is that the photocatalytic activity under visible light is much lower than that under ultraviolet light [10,12]. Therefore, the development of new and optimized photocatalysts exhibiting visible light activity and improved charge carrier dynamics are necessary. In this study, nitrogen doped TiO_2 films are prepared at different deposition pressures, and with different concentrations of nitrogen. Interestingly, the resulting films show a large variance in their optical, morphological, and photoactive properties with significant improvements of the photoactivity observed under visible light irradiation. We investigated the complex synergy between interstitial and substitutional doping, with the competitive effects on the overall photoactive (absorption, photocatalytic, and photoelectrochemical) performance of the films.

2. Experimental

Pure and N-doped TiO_2 thin films were prepared by a RF reactive magnetron sputtering system (SPT 120, Plasmionique). A metallic Ti target (50 mm diameter) having a purity of 99.95%, was sputtered in a reactive gas atmosphere containing Ar, O_2 and N_2 for the deposition of N-doped TiO_2 films, and just Ar and O_2 for the pure TiO_2 films. The deposition pressure was controlled by the Ar flow rate in the deposition chamber, fabricating films at p = 3, 7, and 14 mTorr with corresponding Ar flow rates of 30, 70, and 140 sccm respectively. Different nitrogen to oxygen ratios were used depending on the working pressure. The RF power was 200 W for all the coatings. The fixed experimental conditions chosen were situated in the intermediate region between two stable sputtering modes, reactive and metallic [13,14]. In order to achieve these optimal deposition conditions, the total reactive gas flow rate was fixed at 2.0, 2.3, 2.5 sccm for the samples deposited at 3 mTorr, 7 mTorr, and 14 mTorr, respectively.

The substrate holder was maintained at 300 °C and the distance between the substrate holder and the target was fixed at 10 cm. The films were deposited on several substrates including electro-polished stainless steel (304) for photoelectrochemical and photocatlytic measurements, on Si (1 0 0) wafers for structural and analytical measurements (XRD, SEM, XPS), and ordinary microscope glass slides for optical measurements, we have used the same type of substrate for each type of measurement. Prior to deposition, the substrates were ultrasonically cleaned with acetone, ethyl alcohol and then de-ionized water for 20 min each. After deposition, some of the films were post annealed for 1 h at 450 °C in ambient air.

Optical measurements were carried out by a UV–vis spectrophotometer (Varian 6000). XPS analyses were carried out using Microlab 350 spectroscope (Thermo Fisher Scientific, East Grinstead, UK). Each sample was analyzed using Al Kα X-rays with a non-monochromated radiation at a power of 300 W and a take off angle of 0°. Quantitative analyses were performed using XPSPeak software from peak areas, using the appropriate sensitivity factors. The crystal structure of thin films was characterized by X-ray diffraction (XRD) (X'Pert Pro PW3040-Pro, Panalytical Inc.) using a Cu Kα1 (λ = 1.5418 Å) X-ray radiation source in Bragg–Brentano (θ–2θ) configuration. X'Pert High Score pattern processing was used to collect and process the data.

Photo-electrochemical (PEC) measurements were studied with a voltage controlled potentiostat (Solatron). Reference and counter electrodes used during the PEC measurements were an Ag/AgCl electrode (CHI Instruments/saturated KCl) and a Pt mesh electrode, respectively. The distance between the thin film (working electrode) and the Pt mesh was 25 mm, while the temperature was 25 ± 2 °C. The electrochemical cell had a volume of 15 mL and was filled with 1 M of Na_2SO_4, (Merk). A 125 W (Philips) white lamp was used to irradiate the samples during the photocurrent measurements, and a UV filter was used to cut off all the UV irradiation below 400 nm in order to obtain visible light irradiations at the same light intensity (see Fig. S1 in the Supporting Information).

The photocatalytic activity was evaluated using an aqueous solution of NMP (99%, Merck) with an initial concentration of 10 mg/L at room temperature. The treated solution had a pH adjusted to 3.0 using $HClO_4$ (Sigma–Aldrich, ACS reagent, $\geq$69% (T)). The solution was circulated by a peristaltic pump (MasterFlux, model 7553-75) through the reactor with a flow rate of 5.2 mL/s. The TiO_2 thin film samples, deposited on 50 mm × 50 mm substrates, were placed in the reactor faced to the light irradiation. The treated solution volume was 50 mL and the pH was adjusted to 3.0 using $HClO_4$ (Sigma–Aldrich, ACS reagent, $\geq$69%).

The applied UV source was 11 W Philips TUV low pressure Hg lamp close to monochromatic output at 254 nm and the visible light source was the same as that used for the PEC measurements. The concentration of NMP was analyzed using HPLC (Shimadzu, Lab solutions) with isocratic elution (3–10% acetonitrile, 97–90% water, flow rate: 1 mL min^{-1}) on a reversed-phase Nucleosil C_{18} column. The detection wavelength was set to 214 nm.

3. Results and discussions

The deposition parameters of the various films used for this study are listed in Table 1. The optical band gap calculated by the Tauc model are also presented for the as-deposited and annealed films (at 450 °C). For convenience, we defined the nitrogen ratio for each sample as the ratio of the nitrogen flow rate to the total reactive gas input (oxygen and nitrogen). For example, when the nitrogen flow rate is 0.6 sccm, and the oxygen flow rate is 1.4 sccm, a nitrogen ratio of 30% is used, since nitrogen is 30% of the total reactive gas flow rate (2.0 sccm).

3.1. Film structure and morphology

Fig. 1 presents the SEM images of the TiO_2 samples prepared at deposition pressures of 3 mTorr, 7 mTorr and 14 mTorr. The thickness of the films was estimated by the SEM images to be 465 nm, 435 nm, and 460 nm for the films deposited at 3 mTorr, 7 mTorr, and 14 mTorr, respectively. It was observed that the surface roughness drastically increased as the deposition pressure increased. For example, the film deposited at 3 mTorr revealed a relatively smooth surface, with only a few irregularities observed. For the film deposited at 7 mTorr, the surface roughness increased

Table 1
Samples used in this study with deposition condition, atomic percentage of total nitrogen doping N_{at} as well as of different nitrogen sites (substitutional N_I, chemisorbed N_{II} and interstitial N_{III}) using XPS spectra of N 1s core level. Calculated optical band gaps for as deposited films and annealed films (in bold) are also mentioned. * = low light transmission.

Sputtering parameters				XPS analysis				Optical
$\frac{N_2}{N_2+O_2}$	Deposition pressure (mTorr)	N_2 flow rate (sccm)	O_2 flow rate (sccm)	N_{at} (%)	N_I (%)	N_{II} (%)	N_{III} (%)	E_g (eV)
TiO_2	3	0	2.0	0.3	–	0.3	–	3.5/**3.45**
15%	3	0.3	1.7	0.7	–	0.5	0.2	3.3/**3.28**
25%	3	0.5	1.5	1.0	**0.2**	0.6	0.2	3.18/**3.12**
30%	3	0.6	1.4	3.3	**2.8**	0.2	0.3	2.8/**2.71**
35%	3	0.7	1.3	5.9	**5.2**	0.4	0.3	*/*
TiO_2	7	0	2.3	0.3	–	0.3	–	3.3/**3.26**
26%	7	0.6	1.7	1.1	**0.3**	0.5	0.3	3.25/**3.21**
30%	7	0.7	1.6	3.8	**3.2**	0.4	0.2	2.69/**2.78**
35%	7	0.8	1.5	4.9	**4.1**	0.3	0.5	*/**2.38**
48%	7	1.1	1.2	6.0	**4.9**	0.7	0.4	*/*
TiO_2	14	0	2.5	0.2	–	0.2	–	3.25/**3.23**
40%	14	1.0	1.5	0.7	–	0.4	0.3	3.25/**3.23**
48%	14	1.2	1.3	1.8	**0.3**	1	0.5	3.2/**3.2**
60%	14	1.5	1.0	3.3	**1.6**	0.7	1	2.55/**3.1**
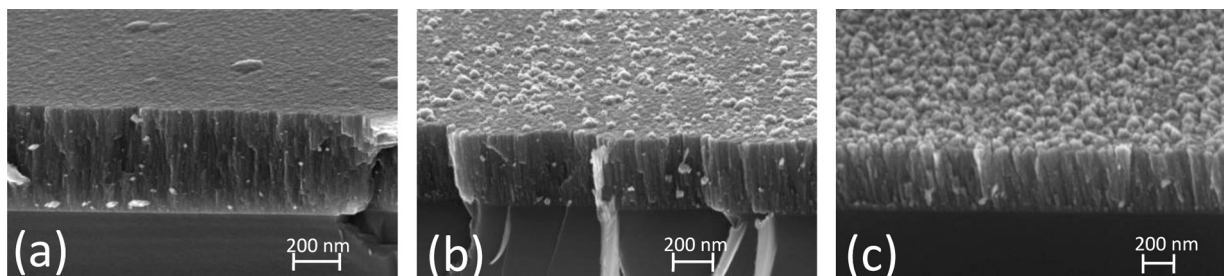
Fig. 1. SEM-FEG images of TiO_2 grown at three different pressures (a) 3 mTorr, (b) 7 mTorr and (c) 14 mTorr.

significantly, and the cracks seen in the cross-sectional SEM images appear to converge at the surface, creating small but substantial holes. When the deposition pressure is increased to 14 mTorr, the film revealed a semi-columnar structure, with the surface porosity continuing from the film surface throughout the bulk to the substrate. In addition to the increased porosity, the formation of clusters on the film surface was seen beginning from 7 mTorr, and also at the higher deposition pressure. The clusters were a result of the increased deposition pressure, which can create semi-large clusters within the deposition plasma, and were then subsequently deposited on the film surface. These clusters should contribute to the formation of higher specific area of the developed surface. The increase of the porosity of the films by increasing the deposition pressure can be explained by the fact that the kinetic energy of the sputtered particles decreases at higher pressure, and therefore the particles reaching the surface should have less energy, less mobility and therefore will give rise to more porous films.

3.2. Film composition and nitrogen doping by XPS

A diverse arrangement in the concentration and nature of nitrogen doping was found throughout the different films. In particular two types of doping could be found; substitutional doping, where nitrogen replaced oxygen in the TiO_2 lattice, and interstitial doping, where nitrogen was bonded to one or more oxygen atom as presented in Table 2. The N 1s core level spectra were measured by XPS, and deconvoluted into three regions: (N_I) between 396 eV to 398 eV, (N_{II}) centered around 400 eV, and (N_{III}) localized at 402 eV. N_I is assigned to substitutional sites of nitrogen detected at binding energy of about 396 eV (O—Ti—N) [15–17], 397 eV (N—Ti—N) [18] and 398 eV (Ti—N—O) [19–21]. N_{II} and N_{III} have many possible assignments but they are widely accepted to correspond to N which is not bonded to Ti. N_{II} is reported

to correspond to chemisorbed N_2 [2,21], however other reports assigned this peak to interstitial nitrogen within TiO_2 [22–24] and substitutional nitrogen [25,26]. A similar peak at 400 eV as N_{II} has been detected in a standard non doped TiO_2, so we assume that the peak N_{II} corresponds to nitrogen in chemisorbed sites. Finally, N_{III} at 402 eV has been attributed to interstitial nitrogen [17,21,27] in the form of (Ti—O—N, NO, or NO_2) and other adsorbed species like N_2 [2,28] or NO dimers [29]. Fig. 2 shows the deconvoluted XPS spectra of the N 1s core level from samples deposited at 14 mTorr for different nitrogen ratio. The calculated atomic concentrations of the main nitrogen sites (N_I), (N_{II}) and (N_{III}) are presented in Table 1, for all the samples.

3.3. Optical properties

The transmission and reflection spectra were measured for each sample before and after annealing at 450 °C in air. The transmission spectra for the annealed films deposited at 7 mTorr are shown in Fig. 3a. The trend for the respective spectra for all

Table 2
Probable nitrogen oxidation states in N doped TiO_2 and the corresponding binding energies.

Binding energy	Type of bonding	Nitrogen oxidation state	References
396 (eV)	N—Ti—O	N^{3-}, N^{2-}	[15–17,30]
397 (eV)	Ti—N triple bonding in TiN	N^{3-}	[5,18,23,30–33,35]
398 (eV)	N—Ti—O (with electron shift from Ti to N) and/or Ti—N—O	N^-	[19–21]
400 (eV)	Chemisorbed N_2 and/or NO_x	N^0, N^+	[21,23,30,34]
402 (eV)	Ti—O—N or Ti—ON	N^+, N^{2+}	[17,21,27]
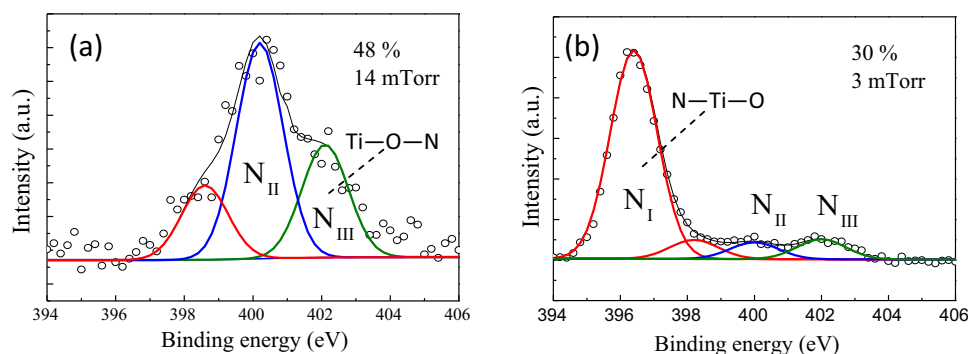
Fig. 2. Deconvolution of N 1s core level spectra for samples showing (a) the best photocatalytic activity and (b) the best photoelectrochemical activity under visible light. Interstitial, chemisorbed and substitutional nitrogen are presented in green, blue and red colors, respectively. (For interpretation of the references to color in this figure legend, the reader is referred to the web version of the article.)

of the as-deposited and annealed samples was similar, showing a distinct shift of the transmission to longer wavelengths as the nitrogen incorporation increased, and the sample with the highest nitrogen ratio had an absorption edge begin at wavelengths higher than $\lambda = 500$ nm. The absorption spectra were calculated using the following equation [36,37],

$$A = \alpha d = \ln\left(\frac{(1-R)^2}{2T} + \left(\frac{(1-R)^4}{4T^2}\right)^{1/2}\right) \quad (1)$$

where A is the absorbance, α is the absorption coefficient, d is the thickness of the sample, R and T are the reflection and transmission spectra, respectively. Then, the effective optical band gaps were also estimated for each sample using the Tauc plots. In order to obtain the estimated optical band gap for the thin films, we plotted $(\alpha h\nu)^{1/2}$ vs. $h\nu$ and the band gap energy was obtained by extrapolating the linear portion of this plot to the intersection with the x-axis ($h\nu$), at which point we determine the band gap. The calculated values of the effective band gaps for the pure and nitrogen doped TiO$_2$ films are shown in Table 1 as well as in Fig. 3b for comparison. The as-deposited and annealed pure TiO$_2$ films showed an estimated band gap energy of $E_g = 3.35 \pm 0.15$ eV, indicative of the anatase phase of TiO$_2$ [38]. As the nitrogen ratio is increased, the band gap is found to decrease in two slopes depending on the deposition pressure (Fig. 3b). This is an expected result, as the introduction of nitrogen, whether substitutional or interstitial, can add stable energy levels within the anatase band gap of TiO$_2$ as well as the formation of TiN structures at higher nitrogen doping (see Section 3.5.2). The formation of TiN crystals in the bulk explains the lowest values of optical transmission and band gap. Therefore, as

more nitrogen was added, the density of nitrogen states within the anatase band gap should increase, and thus more electrons-hole pairs can be excited from within the band gap energy of TiO$_2$. The decrease of the optical band gap energy was observed to depend on the deposition pressure, the change in the slope occurred for nitrogen ratio of 25% and 48% as the films were deposited at lower pressure (3–7 mTorr) and higher pressure (14 mTorr), respectively.

After annealing at 450 °C, the band gap values decreased slightly in general for the low nitrogen doping, which could be explained by the enhancement of crystallinity (increase of the crystal size) and electronic transfer, especially for the dense films prepared at lower pressures. At higher nitrogen doping, we observed an increase of the band gap, that could be explained by the partial reoxidation of nitrogen sites as well as the TiN structures to give oxynitrides. However, this last observation is more pronounced with the films deposited at 14 mTorr which could be probably induced by a faster loss of nitrogen doping (due to the reoxidation of nitrogen sites) in such films [52].

3.4. Valence band observation and analysis by XPS

The difference between the valence band maximum and Fermi level energy can help to describe the electronic structure of pure and N-doped TiO$_2$ films by examining the XPS of O 2p spectra at very low binding energies (near the Fermi level). The valence band spectra of pure and doped thin films are presented in Fig. 4a–c, respectively, for the thin films deposited at 3 mTorr, 7 mTorr and 14 mTorr. The estimated valence band border from the Fermi level has been extrapolated, at the intersection between the 5.4 eV peak (O 2p π-bonding) and the base line [22,45,48]. Within the
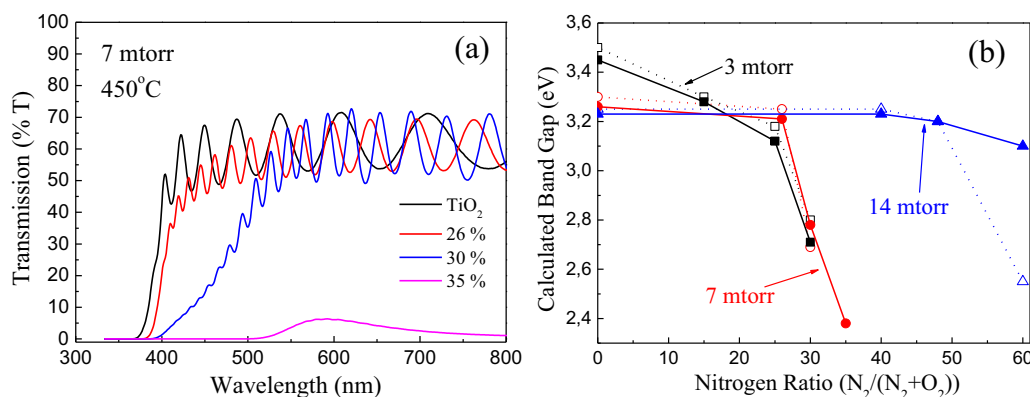
Fig. 3. (a) UV–vis transmission spectra for nitrogen doped samples prepared at 7 mTorr and annealed at 450 °C for 2 h, (b) calculated band gap using Tauc plot for all samples vs. N$_2$% in the reactive gas {N$_2$/(N$_2$ + O$_2$)}, before (dotted line) and after annealing (solid line).
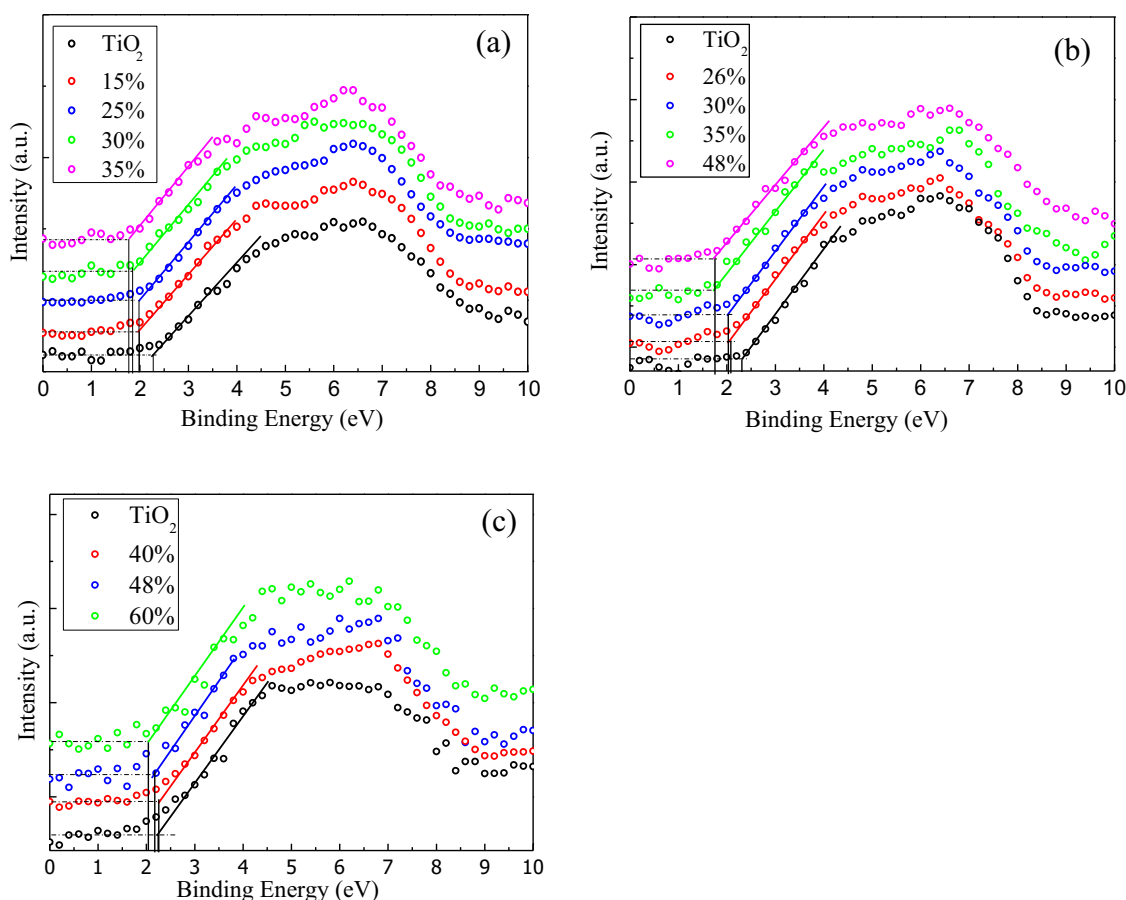
Fig. 4. Valence band using O 2p spectra for different nitrogen flow rate percentage at three different pressures (a) 3 mTorr, (b) 7 mTorr and (c) 14 mTorr.

detection depth of XPS at the surface of the thin film (about 5 nm), no signal associated to Ti^{3+} defect states has been observed near the Fermi level (i.e., there were no oxygen vacancy states that could be detected using the present XPS data) [42,49,50] so the Ti was in its full oxidation state Ti^{4+} at the surface of all the thin films. More details on the behavior of Ti 2p and O 1s are discussed in the Supporting Information.

It was observed that the valance band edge of the non-doped samples was at the same position from the Fermi level (about 2.25 eV) regardless of the deposition pressure. At lower deposition pressures (3–7 mTorr), the overall trend showed that as more nitrogen was incorporated into the films, the valence band border shifted closer toward the Fermi level with a change in the decay slope for nitrogen concentrations higher than 3.3%. This resulted in a decrease of the energy gap between the valence band and the conduction band, with a maximum apparent broadening in the valence band up to 0.5 eV as compared to that of the undoped films. The shift in the valence band edge/Fermi level distance could be due to the domination of substitutional nitrogen doping [17] as mentioned in Table 1. However, the decrease of the distance between the valence band and Fermi level in the 14 mTorr samples was considerably less than the films prepared at lower pressures, as there was significant reduction in the amount of nitrogen at substitutional sites [17].

The decrease in the distance of the valence band from Fermi level energy confirms that the substitutional and interstitial N states lie higher above the O 2p valence band edge. This result is directly correlated to the decrease of the observed optical band gap energy. The XPS and UV–vis observations (see Fig. 3 and Table 1) suggest that at low nitrogen doping ($N_{at} \ll 3.3\%$) the most significant change in the optical properties is due to the broadening of the valence band

energy, which results from the overlap of the O 2p and N 2p orbitals (nitrogen energy states) [51]. However, when the atomic nitrogen doping increases above this critical value, the band gap energies decrease significantly, which is indicative of a higher density of intermediary energy levels within the band gap of TiO_2 [5], which could not be detected clearly by the examination of the XPS data because a Fermi level shifting (toward vacuum level) could take place at higher nitrogen concentration within the doped thin film ($N_{at} \gg 3.3\%$).

3.5. Film Structure versus deposition pressure by XRD

3.5.1. Case of non-doped TiO₂

Fig. 5a presents the XRD scans for the non-doped TiO_2 thin films deposited at three different pressures, 3 mTorr, 7 mTorr and 14 mTorr. An interesting conclusion can be deduced from Fig. 5, taking into account the ratio between the intensities of the peaks corresponding to the two different anatase orientations of titania i.e., (1 0 1) and (0 0 4). It is evident that at lower deposition pressure (3 mTorr), the TiO_2 is more crystallized in the preferential (1 0 1) orientation rather than the anatase (0 0 4), but the latter becomes the preferential orientation as the deposition pressure increases to 7 and 14 mTorr. On the other hand, there is a clear decrease in the anatase XRD intensity at the highest pressure studied (14 mTorr). This can be explained by two facts: (1) a decrease in the TiO_2 crystallinity at higher working pressures which is consistent with the conclusion of Zeman et al. [39], and/or (2) to the reduction in the crystal size (shrinking) when sputtering at higher pressures. The average crystallite size was determined using the Scherrer Formula and presented in the insert of Fig. 5a. The anatase crystal size increases as the deposition pressure increases from 3 mTorr to
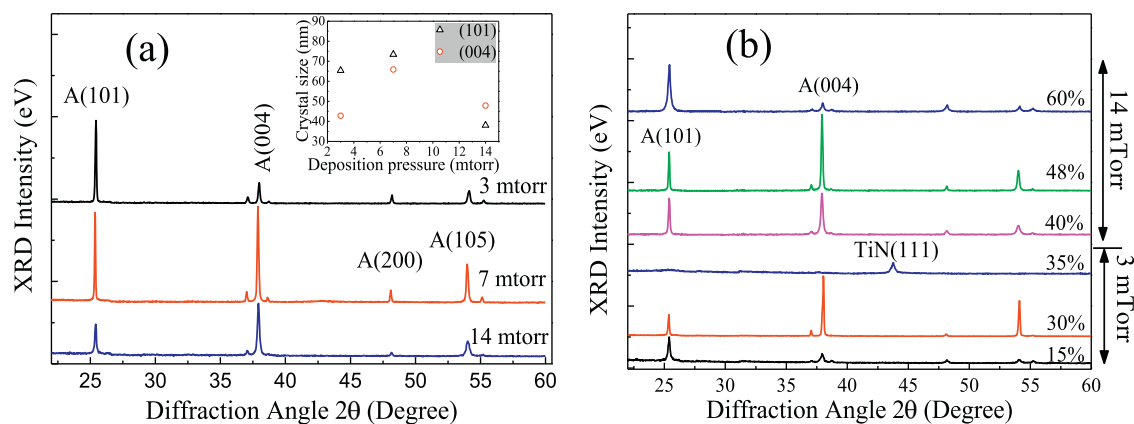
Fig. 5. (a) XRD scan of the pure TiO_2 thin films deposited at 3 mTorr (black), 7 mTorr (red), and 14 mTorr (blue). The insert shows the crystal size of anatase phase (1 0 1) and (0 0 4) vs. deposition pressure, as calculated using Scherrer formula. Samples were post-annealed at 450 °C for 1 h after the deposition. (b) XRD scan of N doped TiO_2 thin films deposited at high and low pressures. (For interpretation of the references to color in this figure legend, the reader is referred to the web version of the article.)

7 mTorr, and a further increase in the deposition pressure induces a decrease in the crystal size.

Crystal size calculations also confirmed the preferential presence of anatase (1 0 1) at low pressure (3 mTorr) and anatase (0 0 4) at high pressure (14 mTorr). However, at an intermediate deposition pressure (7 mTorr) there is almost equal contribution of both (1 0 1) and (0 0 4) orientations accompanied with a general increase in the crystal size.

3.5.2. Case of N-doped TiO_2

The XRD scans for the N-doped films are shown in Fig. 5 b. Doped films prepared at 3 mTorr and 7 mTorr have similar trends, the low nitrogen ratio decreases the crystallinity of the anatase phase of TiO_2, but the high nitrogen ratio makes it easier for TiN to form, and the intermediary nitrogen ratios have a competition between the (1 0 1) and (0 0 4) phases of anatase.

At 3 mTorr, films prepared with nitrogen ratios of 15%, 25%, and 30% all showed diffraction peaks at $2\theta = 25.4°$, and $2\theta = 38°$, corresponding to the (1 0 1) and (0 0 4) orientations of the anatase phase of TiO_2, respectively. The coatings obtained at a lower nitrogen ratio (15%) showed a preferred growth in the (1 0 1) direction of anatase, while the films deposited at 25% and 30% showed stronger preferred orientation in the (0 0 4) direction. The (0 0 4) peak may be partially attributed to an increase in nitrogen incorporation within the TiO_2 lattice. When the nitrogen ratio increases above 35% in the reactive gas, a significant destruction of the anatase phase took place, with a predominance of the TiN crystals in the deposited films. For the films deposited at 7 mTorr, the clear reduction of the anatase phase could be detected when nitrogen ratio reached 35% in the reactive gas but with no predominance of any TiN phases. However, the film deposited at a nitrogen ratio of 48% showed a clear peak corresponding to TiN (1 1 1) at $2\theta = 43.6°$ with no anatase diffraction peaks, reflecting a predominance of the TiN crystals rather than titania or titanium oxynitrides in the structure of the coatings.

A different behavior has been observed with the films deposited at 14 mTorr. The introduction of nitrogen did not quench the growth of the anatase crystals of TiO_2 (up to 60% N). As the nitrogen ratio increased up to 48%, the coating still showed strong anatase characteristics, with dominant peaks found at $2\theta = 38°$, corresponding to the (0 0 4) orientations of the anatase phase. Then, when the nitrogen ratio was further increased (60%), we found a surprising increase in the diffraction peak intensity at $2\theta = 25.4°$ corresponding to a preferential growth in the (1 0 1) orientations of the anatase phase rather than the (0 0 4) one. This result implies that there is a change in the nitrogen incorporation sites when the nitrogen ratio increased from 48% to 60%.

We note also that, in all films deposited at 14 mTorr, there are no diffraction peaks corresponding to any TiN structures, which is not the case in samples prepared at lower pressures. The average crystal size was also investigated by using the Scherrer formula, not presented here. The overall trend for the samples was similar, showing larger crystal sizes at lower nitrogen ratios, which then decreased as the nitrogen ratio increased for all deposition pressures.

3.6. Photoactive properties

Two methods were used to test the photoactivity of pure and N-doped TiO_2; the current generation during photoelectrochemical water splitting reactions, and the photocatalytic degradation of NMP.

3.6.1. Photoelectrochemical performance for water splitting

Fig. 6 presents the electrochemical potentiodynamic scan for N-doped TiO_2 samples deposited at 7 mTorr and irradiated by white light. Films prepared at other pressures had the same overall shape and trends (not shown) as in Fig. 6: the photocurrent first increased with increasing voltage, indicating that charge transfer and recombination occur simultaneously, after then it reached saturation, when charge recombination in the semiconductor could be neglected. The main significant difference between the different samples was the maximum photocurrent density that was generated, which is discussed below.
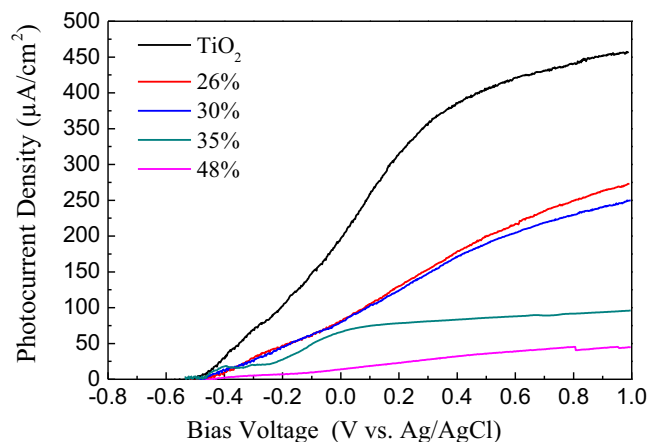
Fig. 6. Electrochemical potentiodynamic sweep under white light irradiation using Ag/AgCl as reference electrode in Na_2SO_4 1 M, pH 7 for N doped samples deposited at 7 mTorr.
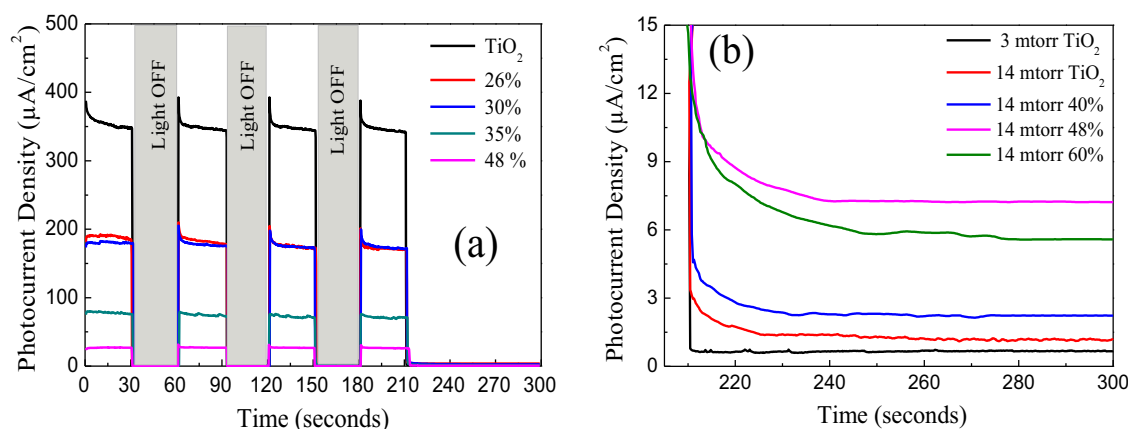
Fig. 7. (a) Example of electrochemical intermittent photocurrent under white light irradiation at a bias voltage of 0.5 V/(Ag/AgCl) in Na$_2$SO$_4$ 1 M, pH 7 for N doped samples deposited at 7 mTorr (b) Visible light photocurrent density for samples deposited at 14 mTorr as compared to TiO$_2$ deposited at 3 mTorr.

The open circuit voltages (V_{OC}) are about −0.15 V, in accordance with the reported data for such pH values [48]. It is well known that titania is a n-type semiconductor with a Fermi level energy close to the conduction band. When the semiconductor is in contact with an electrolyte, whose redox potential is situated in the band gap, an upward bending of the valence and conductive bands is expected, and the TiO$_2$ surface will have a positive charge due to the electronic loss in the depletion region or the charge space [54].

The dark current density slightly increased from 0.3 to 0.6 μA/cm^2 during the positive scan up to 1.0 V. Upon light irradiation, the open circuit voltage (V_{OC}) shifted toward more negative values, respectively about −0.50 V in the white light and −0.30 V in the visible light, for all samples regardless of the deposition conditions. This indicated that for the two different light conditions, the electronic structure has not been significantly affected by the surface morphology or the nitrogen incorporation into the TiO$_2$ films. The photocurrent deviates from the dark current under both white and visible light excitation, although the difference is much greater for white light. This disparity was understandable, because the absorption spectrum for this film showed significantly larger absorbance at UV wavelengths compared to the visible range. The difference between dark current and the photocurrent (under irradiation) quantifies the photo-induced reactions or the oxidation power of the photogenerated holes reaching the TiO$_2$/electrolyte interface. Photo-induced oxidation reactions at TiO$_2$ in aqueous solutions are mainly due to water oxidation, as shown by Fujishima and Honda in their pioneer work [55]. The value of photocurrent can therefore be directly related to the kinetics of O$_2$ generation, though some photo-etching or corrosion phenomena cannot be completely excluded.

Fig. 7 shows the intermittent photocurrent measured at 0.5 V/(Ag/AgCl), in a potential range where saturation of the photocurrent was reached, under white light and visible light irradiations. The samples were alternately irradiated by white light every 30 s followed by 30 s of dark (light OFF). After 210 s, the samples were irradiated by visible light using a UV filter. For simplicity, the intermittent photocurrent densities versus irradiation time are presented only for the samples deposited at 7 mTorr (Fig. 7a). In Fig. 7b, the photocurrent density under visible light is presented for samples deposited at 14 mTorr and we used the data of pure TiO$_2$ deposited at 3 mTorr as reference. The maximum photocurrent generated, at constant voltage of 0.5 V, under white and visible light was plotted in Fig. 8a and b, respectively. When nitrogen was incorporated in the depositions it seemed to degrade the photocurrent generated in the samples prepared at 7 mTorr and 14 mTorr under white light irradiation. However, when these

samples were irradiated under visible light, the addition of nitrogen was not always destructive to the photoactive performance of these films. In particular, a maximum photocurrent was observed at nitrogen ratios of 30% (8.5 μA/cm^2), 25% (3.8 μA/cm^2) and 48% (7.5 μA/cm^2) for films deposited at 3 mTorr, 7 mTorr, and 14 mTorr, respectively. However, for the samples prepared at 3 mTorr, the incorporation of nitrogen produced more photocurrent under white light and visible light illumination. This may result from the combination of the increased nitrogen percentage and the decreased porosity of this film. This trend indicates that the incorporation of nitrogen into the films prepared at pressures above 3 mTorr is destructive to the UV induced photoelectrochemical performance, but enhances the visible light reactivity.

The maximum photocurrent density was found to depend on the deposition pressure as well as the doping level. In general, the samples prepared at 3 mTorr showed the highest photocurrent density, with a peak photocurrent achieved when the nitrogen ratio was 25% (N$_{at}$ = 1%) under white light irradiation, and at 30% (N$_{at}$ = 3.3%) under visible light irradiation. A maximum white light photocurrent density of 567 μA/cm^2, 347 μA/cm^2 and 99 μA/cm^2 was measured at nitrogen ratios of 25% (3 mTorr), 0% (7 mTorr), and 0% (14 mTorr), respectively.

When interstitial and substitutional nitrogen sites were both observed in the same sample, it seemed to have a synergic effect on the electrochemical properties, especially at lower nitrogen concentrations (N at.% < 3.3), where the maximum photocurrent density under UV and visible light irradiation was observed. At higher nitrogen concentrations (N at.% > 3.3), the concentration of substitutional nitrogen sites increased, which decreased both visible and UV light photocurrent density regardless of the deposition pressure.

Under visible light irradiation, the decrease of the photocurrent density was observed when substitutional nitrogen was dominant, as well as with the formation of the TiN structure. The introduction of TiN into the films was found to have two dramatic effects: first, TiN is not inherently photoactive and it reduces the photo-generation efficiency of the charge carriers due to the destruction of the anatase TiO$_2$ crystal lattice, and second, they act as recombination centers for the photo-generated electrons and holes.

3.6.2. Photocatalytic activity

N-methyl-2-pyrrolidone (NMP), a cyclic nitrogen-containing organic chemical, is a versatile solvent and reaction medium. It has found wide use in petrochemical, plastic, coating, agricultural, and electronic industries because of its low volatility, thermal stability, high polarity and aprotic, noncorrosive properties [40–43].
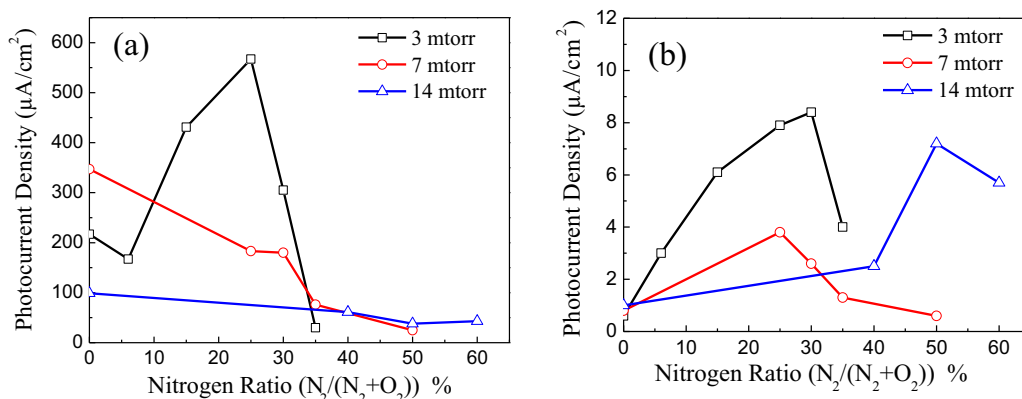
Fig. 8. Photocurrent density under (a) white light and (b) visible light irradiations at a bias voltage of 0.5 V/(Ag/AgCl) in Na_2SO_4 1 M, pH 7 for all N doped samples deposited at different pressures vs. N_2% in the reactive gas.

Therefore, it has been found in the wastewater of many industries. Conventional wastewater treatment methods such as chemical precipitation, activated carbon adsorption, and ion-exchange processes can effectively remove organic compounds from wastewater [40,41]. However, the contaminants are transferred from one medium to another by these methods, and hence further treatment or disposal is required. In addition, the biodegradation of NMP is not only slow but also the product of the degradation is a carbonyl compound, which has a significant COD and cannot be broken down further under normal conditions of sewage treatment [42,43]. Here, we decompose NMP via photocatalysis over N-doped TiO_2 thin films under UV light and also under visible light alone, demonstrating interesting use of this technique. This process irreversibly breaks down the NMP molecules, and provides a safe method to effectively remove this pollutant from wastewater.

Fig. 9 shows the concentrations of NMP as a function of time during the UV photodegradation with different doped samples deposited at 14 mTorr and pure TiO_2 deposited at 3 mTorr. From Fig. 9, it is clear that even with the blank substrate, the concentration of NMP decreased due to UV photo-bleaching. However, when TiO_2 and N-doped TiO_2 samples were inserted, the degradation kinetics increased significantly. Fig. 10 presents the percentage of degraded NMP in the aqueous solution, with the presence of the different studied samples, after 6 h of visible light irradiation. When looking at Figs. 9 and 10, it is clear that the most efficient photocatalytic activity was found for the samples prepared at 14 mTorr as

compared to the films prepared at other pressures which is consistent with our previous work [44]. In particular the sample prepared with a nitrogen ratio of 48% gave the best photocatalytic activity under UV irradiation, but the films prepared with 48% and 60% nitrogen ratios gave the best photocatalytic activity under visible irradiation. The two major parameters which affected the photocatalytic performance were the film morphology and nitrogen doping sites. As was discussed in Section 3.1, the deposition pressure had a significant effect on the films morphology. In particular as the deposition pressure increased, the developed surface of the films also increased giving more active catalytic sites for photocatalysis to take place. The other factor which played a role in the photocatalytic functionality of the films was the nitrogen doping sites. It was observed that as the interstitial nitrogen sites increased, the photocatalytic activity became higher. Then as the substitutional nitrogen started to become dominant, the UV activity decreased again but not the visible one [53], as shown by the film prepared at a nitrogen ratio of 60% (see Table 1). This could be a direct result of the change in the photogenerated charge separation, with the porous films having more interstitial nitrogen doping than substitutional nitrogen sites. However, when substitutional nitrogen became dominant there was a probable recombination between the UV generated electron–holes which explains the reduction of the UV photocatalytic activity with the sample prepared at 14 mTorr
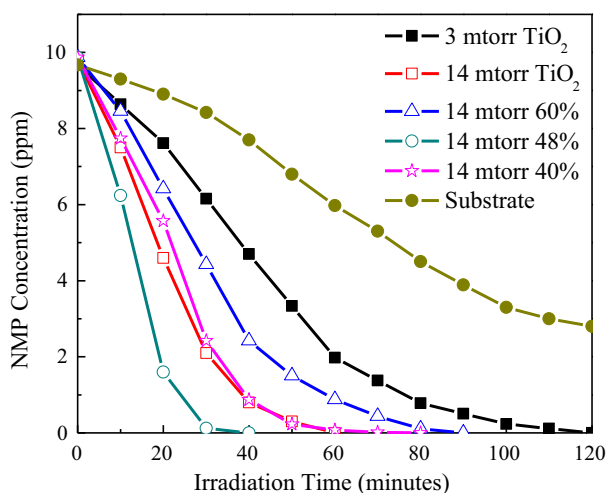
Fig. 9. Kinetic of NMP degradation under UV light using some selected N doped samples deposited at 14 mTorr and 3 mTorr.
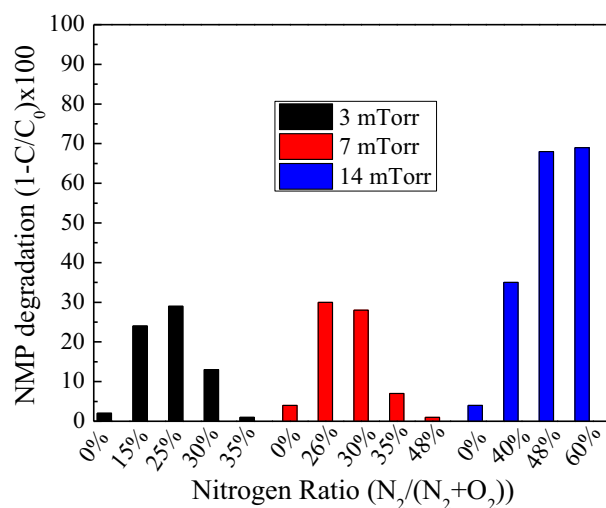
Fig. 10. Efficiency of NMP degradation under visible light using pure TiO_2 (0%) and N doped samples deposited at 3 mTorr, 7 mTorr and 14 mTorr. C and C_0 being the initial concentration (10 ppm) and the final concentration, respectively, of NMP.

Table 3
Optimal deposition pressure and atomic percentage of nitrogen within doped TiO_2 for photocurrent generation and photocatalyse, using UV and/or visible light excitation.

	Photocurrent density	Photocatalytic activity
Visible light	3 mTorr/N_{at} 3.3%	14 mTorr/N_{at} >1.8%
UV light	3 mTorr/N_{at} 1%	14 mTorr/N_{at} 1.8%

with nitrogen ratio of 60%. This is in partial agreement with the work of Yates et al. [30] and other works [19,45–47] who found that nitrogen in chemisorbed and interstitial states doping were more efficient for photocatalytic efficiency rather than substitutional nitrogen doping.

3.6.3. Correlation between the photo responses and the different nitrogen sites

In the Supporting Information, we presented the correlation between three different photo responses (optical band gap E_g, visible photocatalytic activity PCA and the visible photo-electrochemical current PEC) and the atomic concentration of the N_I and N_{III} nitrogen sites for the different deposition pressures. It was found that PCA, PEC and E_g change independently from the concentration of N_{II}. That means, nitrogen present in chemisorbed sites (N_{II}) does not affect any photoresponses. The PCA and PEC efficiencies increase as N% increases up to reaching to an optimal concentration of atomic N in the structure. This optimal concentration of nitrogen is almost independent of the deposition pressure and it is found to be less than 3% at. Then, if the concentration of nitrogen increases further, the PCA and PEC photo efficiencies are found to decrease. More interestingly, the photoactivity of N doped TiO_2 decreases dramatically when the substitutional nitrogen sites exceed largely the concentrations of the interstitial nitrogen sites. This is a direct and important conclusion of this study.

As seen before in the section of optical properties, the band gap decreases as the concentration of nitrogen increases, especially when the substitutional nitrogen sites dominate the other nitrogen species in the thin film.

3.6.4. Comparison between photocatalysis and water splitting

It is interesting to note that the optimal properties of the films are not the same for the water splitting PEC and photocatalysis PCA as shown in Table 3. This could be explained by the effect of different nitrogen sites. Nitrogen at interstitial sites is found to be more efficient for the photocatalytic activity, but when the substitutional sites (N_I) became dominant it had a negative effect on PCA especially under UV light. However, these substitutional sites N_I are efficient for the photoelectrochemical activity if N at.% < 3.3%. These results imply that the deposition conditions and doping parameters have different functionalities for the resulting films, and thus can be tuned dependent on the type of desired application. For the electrochemical and optoelectronic applications, the films deposited at 3 mTorr with low nitrogen doping (1 at.% and 3.3 at.% under UV light and visible light respectively) are more photoactive than those deposited at higher pressure because the films produced at lower pressure have a higher density. The photocatalytic degradation of NMP was found to be the highest for the films prepared at 14 mTorr with a nitrogen doping of 1.8 at.% under UV irradiation. However, for visible irradiations, the optimal photoactive performance was found in the samples with 3.3% of atomic nitrogen doping. The difference between the optimized TiO_2:N films, under UV and visible light, could be explained by the reduction of the generation of electron–hole under the UV irradiation and/or the recombination between the generated electron–hole at higher nitrogen doping ratio. In fact, when nitrogen is doped within TiO_2 it can increase the visible light absorption (due to the new N energy states in the

gap) but also it can limit the UV light penetration and absorption due to the reduction in the anatase phase of TiO_2 in the film structure as confirmed by XRD data. The compromise between these two trends depends on the type of photo generated electron–hole pairs whether from UV or visible light. The introduction of deeper nitrogen states (>0.3 eV above the top of the valence band) could act as a trapping and/or recombination centers of the charge carriers. The difference between the optimized TiO_2:N films, under UV and visible light, show that any improvement of the visible light activity of the films due to nitrogen doping will reduce the corresponding same activity in UV. However, since the proportion of UV in the case of solar applications is only 2%, it is possible to improve the global photoactivity of the films by carefully reducing the photoactivity in UV if the corresponding gain in visible is superior to the former.

4. Conclusions

This study has shown the ability to tailor nitrogen doped TiO_2 films with controllable morphology, optical properties, and photoactive performance. Interestingly, the optimal deposition and doping conditions depend closely on the type of the desired application of the coatings and on the photo-excitation source. The desired impurity energy level(s) introduced in the electronic band gap of TiO_2 by nitrogen doping do not necessarily improve the photocatalytic activity, despite the desired optical properties observed (decrease of the band gap). The decrease in PCA is probably due to the active recombination sites produced, depending on the complexity of the nanoscale surface. Interstitial nitrogen doping sites seem to improve the photocatalytic activity of TiO_2, rather than substitutional sites, due to the better charge separation especially with porous films having an active surface area much higher than the projected surface. The synergic effect of substitutional and interstitial nitrogen sites are more efficient to improve the electrochemical photoactivity of TiO_2 due to the good light absorption, charge transfer in substitutional doping, and the good charge separation induced by the interstitial nitrogen doping. Furthermore the contradictions found reported in the literature concerning nitrogen doping sites and the different photo-activities of N doped TiO_2 were discussed. This work showed that the doping parameters must be tuned depending strongly on the type of the desired application. In the case of solar applications, it is possible to improve the global photoactivity of the films by carefully reducing the photoactivity in UV if the corresponding gain in visible is superior to the former.

Appendix A. Supplementary data

Supplementary material related to this article can be found, in the online version, at http://dx.doi.org/10.1016/j.apcatb.2013.06.028.

References

[1] F. Han, V.S.R. Kambala, M. Srinivasan, D. Rajarathnam, R. Naidu, Applied Catalysis A 359 (2009) 25–40.

[2] R. Asahi, T. Morikawa, T. Ohwaki, K. Aoki, Y. Taga, Science 293 (2001) 269–271.
[3] S.U.M. Khan, M. Al-Shahry, W.B. Ingler, Science 297 (2002) 2243–2245.
[4] R. Beranek, B. Neumann, S. Sakthivel, M. Janczarek, T. Dittrich, H. Tributsch, H. Kisch, Journal of Chemical Physics 339 (2007) 11–19.
[5] C. Di Valentin, E. Finazzi, G. Pacchioni, A. Selloni, S. Livraghi, M.C. Paganini, E. Giamello, Journal of Chemical Physics 339 (2007) 44–56.
[6] S. Lee, E. Yamasue, K. Ishihara, H. Okumura, Applied Catalysis B 93 (2010) 217–226.
[7] A. Zaleska, Recent Patents on Engineering 2 (3) (2008) 158–164.
[8] Y. Nakano, T. Morikawa, T. Ohwaki, Y. Taga, Journal of Chemical Physics 339 (2007) 20–26.
[9] M. Kitano, M. Matsuoka, M. Ueshima, M. Anpo, Applied Catalysis A 325 (2007) 1–14.
[10] H. Irie, Y. Watanabe, K. Hashimoto, Journal of Physical Chemistry B 107 (2003) 5483–5486.
[11] B. Liua, L. Wena, X. Zhao, Solar Energy Materials and Solar Cells 92 (2008) 1–10.
[12] H. Yu, X. Zheng, Z. Yin, F. Tag, B. Fang, K. Hou, Chinese Journal of Chemical Engineering 15 (6) (2007) 802–807.
[13] W.D. Sproul, D.J. Christie, D.C. Carter, Thin Solid Films 491 (2005) 1–17.
[14] A. Brudnik, M. Bucko, M. Radecka, A. Trenczek-Zajac, K. Zakrzewska, Vacuum 82 (2008) 936–941.
[15] N. Raut, T. Mathews, S. Rajagopalan, R. Subba Rao, S. Dash, A. Tyagi, Solid State Communications 151 (2011) 245–249.
[16] Z. Zhang, J.B.M. Goodall, D.J. Morgan, S. Brown, R.J.H. Clark, J.C. Knowles, N.J. Mordan, J.R.G. Evans, A.F. Carley, M. Bowker, J.A. Darr, Journal of the European Ceramic Society 29 (2009) 2343–2353.
[17] P. Romero-Gomez, S. Hamad, J.C. Gonzalez, A. Barranco, J.P. Espinos, J. Cotrino, A.R. Gonzalez-Elipe, Journal of Physical Chemistry C 114 (2010) 22546–22557.
[18] A. Trenczek-Zajac, M. Radecka, K. Zakrzewska, A. Brudnik, E. Kusior, Journal of Power Sources 194 (2009) 93–103.
[19] F. Peng, Y. Liu, H. Wang, H. Yu, J. Yang, Chinese Journal of Chemical Physics 23 (4) (2010) 437–441.
[20] J. Sun, L. Qiao, S. Sun, G. Wang, Journal of Hazardous Materials 155 (2008) 312–319.
[21] S. Lee, I. Cho, D.K. Lee, D.W. Kim, T.H. Noh, C.H. Kwak, S. Park, K.S. Honga, J.K. Lee, H.S. Jung, Journal of Photochemistry and Photobiology A 213 (2010) 129–135.
[22] J. Wang, D.N. Tafen, J.P. Lewis, Z. Hong, A. Manivannan, M. Zhi, M. Li, N. Wu, Journal of the American Chemical Society 131 (2009) 12290–12297.
[23] G. He, L. Zhang, G. Li, M. Liu, X. Wang, Journal of Physics D: Applied Physics 41 (2008), 045304 1–9.
[24] O. Diwald, T.L. Thompson, E.G. Goralski, S.D. Walck, J.T. Yates, Journal of Physical Chemistry B 108 (1) (2004) 52–57.
[25] X. Chen, C. Burda, Journal of Physical Chemistry B 108 (2004) 15446–15449.
[26] X. Chen, Y.B. Lou, A.C.S. Samia, C. Burda, J.L. Gole, Advanced Functional Materials 15 (2005) 41–44.
[27] N.T. Nolan, D.W. Synnott, M.K. Seery, S.J. Hinder, A.V. Wassenhoven, S.C. Pillai, Journal of Hazardous Materials 211 (2012) 88–94.
[28] R. Andrievski, Z. Dashevsky, G. Kalinnikov, Technical Physics Letters 30 (2004) 930–932.
[29] T. Herranz, X. Deng, A. Cabot, Z. Liu, M. Salmeron, Journal of Catalysis 283 (2011) 119–123.
[30] H.M. Yates, M.G. Nolan, D.W. Sheel, M.E. Pemble, Journal of Photochemistry and Photobiology A 179 (2006) 213–223.
[31] R. Parra, A. Arango, J. Palacio, Dyna 77 (163) (2010) 64–74.
[32] H. Kawasaki, T. Ohshima, Y. Yagyu, Y. Suda, S.I. Khartsev, A.M. Grishin, Journal of Physics: Conference Series 100 (2008), 012038 1–4.
[33] B. Avasarala, P. Haldar, Electrochimica Acta 55 (28) (2010) 9024–9034.
[34] A. Emeline, V. Kuznetsov, V. Rybchuk, N. Serpone, International Journal of Photoenergy 2008 (2008), 258394 1–19.
[35] M. Wong, H. Chou, T. Yang, Thin Solid Films 494 (2006) 244–249.
[36] A. Salem, Y. El-Gendy, G. Sakr, W. Soliman, Journal of Physics D: Applied Physics 41 (2008) 025311.
[37] Y. El-Gendy, Journal of Physics D: Applied Physics 42 (2009) 115408.
[38] D. Hanaor, C. Sorrell, Journal of Materials Science 46 (2011) 855–874.
[39] P. Zeman, S. Takabayashi, Surface and Coatings Technology 153 (2002) 93–99.
[40] M. Chong, B. Jin, C. Chow, C. Saint, Water Research 44 (10) (2010) 2997–3027.
[41] S. Pardeshi, A. Patil, Journal of Hazardous Materials 163 (2009) 403–409.
[42] M. Batzill, E.H. Morales, U. Diebold, Journal of Chemical Physics 339 (2007) 36–43.
[43] S. Chow, Water Research 17 (1983) 117–118.
[44] H. Fakhouri, W. Smith, J. Pulpytel, A. Zolfaghari, H. Mortaheb, F. Meshkini, R. Jafari, F. Arefi-Khonsari, Journal of Nano- and Electronic Physics 3 (1) (2011) 26–40.
[45] F. Dong, W. Zhao, Z. Wu, S. Guo, Journal of Hazardous Materials 162 (2009) 763–770.
[46] H. Shen, L. Mi, P. Xu, W. Shen, P. Wang, Applied Surface Science 253 (2007) 7024–7028.
[47] S.H. Lee, E. Yamasue, H. Okumura, K.N. Ishihara, Applied Catalysis A 371 (2009) 179–190.
[48] A. Fujishima, X. Zhang, D.A. Tryk, Surface Science Reports 63 (2008) 515–582.
[49] C. Chusuei, W. Goodman, Langmuir 26 (2010) 921–938.
[50] S. Wendt, P. Sprunger, E. Lira, G. Madsen, Z. Li, J. Hansen, J. Matthiesen, A. Blekinge-Rasmussen, E. Lægsgaard, B. Hammer, F. Besenbacher, Science 320 (2008) 1755–1759.
[51] Z. Zhao, Q. Liu, Journal of Physics D: Applied Physics 41 (2008), 085417 1–10.
[52] W. Smith, H. Fakhouri, J. Pulpytel, S. Mori, R. Grilli, M.A. Baker, F. Arefi-Khonsari, Journal of Physical Chemistry C 116 (30) (2012) 15855–15866.
[53] Y. Nosaka, M. Matsushita, J. Nishino, A.Y. Nosaka, Science and Technology of Advanced Materials 6 (2005) 143–148.
[54] A. Bott, Current Separations 3 (1998) 87–91.
[55] A. Fujishima, K. Honda, Nature 238 (1972) 37–38.